Mikailalsys Journal of Mathematics and Statistics

e-ISSN : 3030-816X
p-ISSN : 3030-8399

Index : Harvard, Boston, Sydney University, Dimensions, Lens, Scilit, Semantic, Google, etc

https://doi.org/10.58578/MJMS.v4i2.9387

Semi-Analytical Study of Pulsatile Nanofluid Flow in Porous Stenosed Arteries Under Magnetic and Thermal Effects

Ali Musa[1] & D.G Yakubu[2]
[1]Yobe State University Damaturu, Nigeria
[2]Abubakar Tafawa Balewa University, Bauchi, Nigeria
isahabdullahi7474@gmail.com

Article Info:

Submitted:	Revised:	Accepted:	Published:
Feb 8, 2026	Mar 8, 2026	Mar 20, 2026	Mar 25, 2026

Abstract

This study presents an extended fractional Maxwell fluid model for pulsatile blood flow through a stenosed artery by incorporating the combined effects of a magnetic field, porous medium, chemical reaction, heat source, and suspended nanoparticles. Blood is modeled as a compressible, viscoelastic, and electrically conducting fluid, and the governing fractional-order coupled nonlinear partial differential equations for momentum, energy, and nanoparticle concentration are formulated in cylindrical coordinates. To capture fluid memory effects, the Caputo fractional derivative is employed, and the resulting system is solved semi-analytically using the Laplace transform method. The inverse Laplace transforms, involving modified Bessel functions, are computed numerically through the Concentrated Matrix-Exponential method implemented in Python to improve stability and accuracy. Validation against existing literature demonstrates excellent agreement. The parametric results show that increasing the Hartmann number, stenosis length, particle mass, and chemical reaction parameter reduces both velocity and nanoparticle concentration, whereas higher heat source, Peclet number, and nanoparticle

concentration parameters enhance flow and particle dispersion. The findings further indicate that fractional-order effects strongly influence velocity behavior, with lower fractional orders producing stronger memory effects and smoother gradients. The study concludes that the proposed model improves the prediction of hemodynamic behavior under pathological arterial conditions and offers useful implications for magnetic-assisted therapies and nanoparticle-based drug delivery.

Keywords: Fractional Maxwell Fluid; Pulsatile Blood Flow; Stenosed Artery; Magnetohydrodynamics; Nanoparticle Transport

Introduction

Blood is a vital biological fluid in the human body, circulating continuously through blood vessels due to the heartbeat and playing a crucial role in metabolism. Insufficient blood flow can lead to metabolic disturbances and tissue damage. Recent studies have indicated that magnetic fields can positively impact various human systems, including the cardiovascular system. As a result, significant research has focused on the effects of magnetic fields (MF) on blood flow within vessels (Ganguly *et al.,* 2005). For instance, an experiment by Haik et al., 2001 found that blood flow decreases by 30% under a 10T high magnetic field due to an increase in the blood's apparent viscosity caused by the MF. Shit et al. explored blood flow in a constricted artery, considering the impact of body acceleration and the Lorentz force. Earlier research by MacDonald and Caro1974 suggested that blood behaves as a Newtonian fluid, which only holds true for flow under high shear rates in larger vessels. However, experiments have shown that blood exhibits non-Newtonian characteristics at lower shear rates, even in large arteries. Using a Newtonian fluid model, Ogulu *et al.,*2007 derived the analytical solution for oscillatory blood flow in various blood vessels under the influence of MF. Tzirtzilakis 2015 numerically studied the flow of blood modeled as a Newtonian magnetic fluid through an aneurysm using finite difference methods, while Tabi et al. derived exact solutions for nonlinear equations governing blood flow and heat transfer in large vessels under MF and radiation. More recently, Zaman *et al.*2015 examined unsteady blood flow through a stenosed channel with a w-shaped curve, incorporating magnetohydrodynamics and entropy generation. Numerous studies have also focused on blood flow modeled as a non-Newtonian fluid. For example, Ali *et al.,*2015 used a Carreau model to characterize the unstable flow of blood in a stenosed artery with body

acceleration and MF. Ghasemi *et al.,*2016 applied the Differential Quadrature Method to solve non-Newtonian blood flow in coronary and femoral arteries. Padma *et al.*2019 modeled pulsatile blood flow in a tapered vessel with slight constriction, incorporating magnetic nanoparticles, electric force, and Lorentz force**.**

Motivated from the above background, this study is concerned with developing an efficient semi analytical method to derive the solution of unsteady oscillatory blood flow pass a small stenosed vessel caused by a pulsatile pressure gradient, thermal radiation together with a uniform MF. Since the shear rate is relatively low in small vessels, a non-Newtonian fluid model, i.e., fractional Maxwell fluid model, is supposed for simulating rheological behavior of blood.

The study of blood flow through small arteries has garnered increasing attention due to its relevance in diagnosing and treating cardiovascular diseases. Existing models, such as the one previously developed by (Wang et al., 2022), have significantly contributed to understanding the fluid dynamics of blood in the presence of magnetic fields, and associated thermal and mass transfer effects. However, the biological and physical environment of human blood vessels is far more complex than what current models capture. Notably, factors such as internal heat generation (heat source), tissue porosity, chemical reactions due to medication or metabolic processes, and the presence of nanoparticles (used in targeted drug delivery or diagnostic imaging) can significantly alter blood flow behavior, temperature distribution, and mass transport characteristics. The inclusion these parameters is vital in simulating realistic thermal behavior arising from metabolic heat generation, essential modeling to simulate blood flow through partially blocked or degenerated tissue layers, which is a common condition in advanced arterial diseases such as stenosis. Furthermore, the suspension of nanoparticles in blood either introduced externally or occurring naturally significantly influences viscosity, thermal conductivity, and mass diffusivity, hence affecting the flow and transport phenomena in critical ways.

Therefore, based on the aforementioned rationales, this study proposes an extended mathematical model to investigate the combined effects of heat source/sink, porosity, chemical reactions, and nanoparticles on unsteady blood flow through an artery with composite stenosis under the influence of a magnetic field, heat, and mass transfer. This model aims to provide a more comprehensive and realistic representation of

physiological conditions and contribute to improved biomedical engineering designs and clinical therapies related to cardiovascular health.

Methodology

Formulation of Problem

In this study, we examine the behavior of a compressible, axially symmetric, unsteady blood flow within a stenosed artery, accounting for complex physiological and physical effects. The artery is modeled as a cylindrical tube with an axisymmetric stenosis (narrowing), which is a common pathological condition in cardiovascular systems. To simulate realistic biomedical conditions, blood is treated as a non-Newtonian viscoelastic fluid using a fractional Maxwell model. This choice reflects the complex rheological behavior of blood, especially under low shear rates found in small or stenosed arteries. In addition to its inherent viscoelastic nature, the blood is considered to carry suspended nanoparticles (e.g., copper, gold, or aluminum oxide), enhancing its thermal and mass transport properties. The geometric parameters defining the artery include r: the radial coordinate,

z: the axial coordinate along the artery's length, and R(z): the stenosis shape function defining local reduction in radius. The collective influence of these parameters on the dynamics of fluid flow is illustrated in Figure 1.

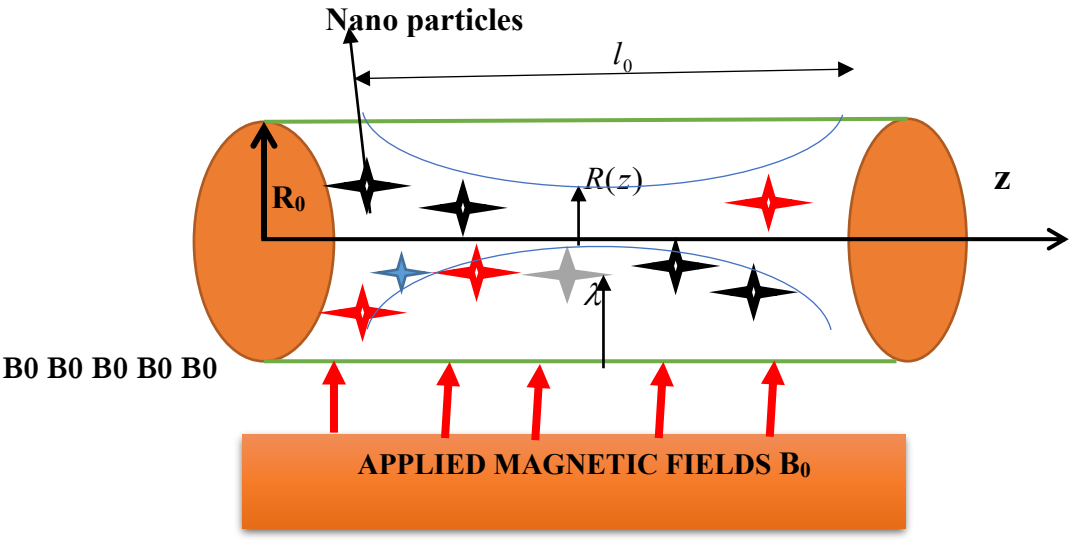

Figure 1: Flow Geometry of the Stenosed Artery

The geometry of the stenosed region is specified using a shape function $R(z)$, as described in Equation (10) of Section 2.2. This function defines the varying arterial radius along the axial direction, characterized by maximum stenosis height λ and stenosis length l_0. An external transverse magnetic field B_0 is applied perpendicular to the flow direction. The magnetic field interacts with the electrically conducting blood to produce a Lorentz force, which resists the motion and modifies velocity profiles.

Governing Equations

The mathematical formulation governing the blood flow consists of a set of coupled, nonlinear, fractional partial differential equations that describe the Momentum, Energy and Concentration equation as referenced in (Wang et al., 2022, and Yakubu et al.,2025) is given by:

$$\rho\frac{\partial\bar{u}}{\partial\bar{t}} = -\frac{\partial\bar{p}}{\partial\bar{z}} + \frac{1}{r}\frac{\partial}{\partial r}(r\tau_{rz}) + \rho G(\bar{t}) + KN(\bar{v}-\bar{u}) + g\beta(T-T_0\bar{)} - \sigma B_0^2\bar{u} + g\beta'(C-C_0\bar{)} - \frac{\bar{u}}{\bar{k}}\Big\} \quad (1)$$

$$\rho C_\rho\frac{\partial\overline{T}}{\partial\bar{t}} = k_T\frac{\partial}{\partial r}(r\frac{\partial\overline{T}}{\partial\bar{r}}) - \frac{\partial\bar{q}}{\partial\bar{y}} + Q(T-T_0\bar{)} + \sigma B_0^2\bar{u}^2 + \mu(\frac{\partial u}{\partial r})^2 \quad (2)$$

$$m\frac{\partial\bar{v}}{\partial\bar{t}} = k_s(\bar{u}-\bar{v}) \quad (3)$$

$$\frac{\partial\overline{C}}{\partial\hat{t}} = D\left(\frac{\partial^2\overline{C}}{\partial\bar{r}^2} + \frac{1}{\bar{r}}\frac{\partial\overline{C}}{\partial\bar{r}}\right) - A(\overline{C}-\overline{C}_0) \quad (4)$$

Pulsatile flow is essential from both physiological and mathematical perspectives for accurately representing blood flow behavior in arteries, particularly when subjected to external vibrations, oscillatory pressures, or thermal influences. As described in (Shirt et al., 2015 & Ellahi et al., 2019), this pulsatile characteristic is modeled using time-periodic functions that account for body acceleration, pressure gradient, and thermal radiation within a vibrational environment, respectively, as follows;

$$G(\bar{t}) = \bar{A}_0\cos(k\bar{t}+\Phi) \quad (5)$$

$$-\frac{\partial\bar{p}}{\partial\bar{z}} = \bar{a}_0 + \bar{a}_1\cos(\bar{\omega}\bar{t}) \quad (6)$$

$$-\frac{\partial q}{\partial\bar{r}} = 4\alpha^2\left(\overline{T}-\overline{T}_0\right) \quad (7)$$

The symbols $\rho, \bar{t}, \bar{r}, \bar{p}, \mu, K, \sigma, g, \beta_T, \beta_C, \overline{T}, \overline{T}_0, \overline{C}, \overline{C}_\infty, k, D, C_p, Q, k_T, B_0, \bar{u}, \bar{v}, a_0, a_1, \Phi, \omega$, and A_0 have been properly defined in Table 1.

Table 1. Nomenclature

Symbol	Description	Unit
D	Mass diffusivity	m^2/s
C_p	Specific heat capacity	$jkg^{-1}K^{-1}$
u_{z0}	Reference velocity	m/s
k	thermal conductivity	$Wm^{-1}K^{-1}$
θ	Dimensionless temperature	K^{-1}
ϕ	Dimensionless concentration	mol/dm^3
ρ	Density	kg/m^3
σ	Electrical Conductivity	m^2/s
μ	Dynamic viscosity	Pas
g	Gravitational acceleration	m/s^2
β_T	Thermal expansion	K^{-1}
β_C	Mass expansion	$kg^{-1}m^3$
B_0	Magnetic field	T
r	Radial Coordinate	m
a_0, a_1	Stenosis amplitude parameter	–
A_0	Dimensional amplitude of applied field	A/m
T_0	Free stream temperature	K^{-1}
Φ	Phase angle	$(^0)$
C	Solutes concentration	mol
C_∞	Free stream concentration	mol
u	Blood Velocity	m/s
v	Velocity of the nanoparticle	m/s
Q	Amount of heat	$Joule$
T	Wall temperature	K^{-1}

According Adamu *et al*., (2020), the Cauchy stress tensor, τ_{rz} is defined as;

$$\tau_{rz} = \mu \frac{1}{\left(1+\lambda_1^{\alpha} D_t^{\alpha}\right)} \frac{\partial}{\partial r} u(r,t). \tag{8}$$

The above equations are governed by the corresponding initial and boundary conditions.

$$\left.\begin{array}{llll} \bar{u} = \bar{u}_0, \overline{T} = \overline{T}_0, \overline{C} = \overline{C}_0; & \forall \bar{r} \in (0.R_0), & at & \bar{t} = 0 \\ \dfrac{\partial \bar{u}}{\partial \bar{r}} = 0, \dfrac{\partial \overline{T}}{\partial \bar{r}} = 0, \dfrac{\partial \overline{C}}{\partial \bar{r}} = 0; & \forall t > 0, & at & \bar{r} = 0 \\ \bar{u} = 0, \overline{T} = \overline{T}_w, \overline{C} = \overline{C}_0; \forall \bar{t} > 0 & & at & \bar{r} = \overline{R}(\bar{z}) \end{array}\right\} \tag{9}$$

The symbols $\bar{u}_0, \bar{T}_0, \bar{C}_0,$ maintained their usual meaning, and $\bar{R}(\bar{z})$ represent the equation that models the stenosed region, as stated in (Imoro et al.,2024) as follows:

$$\bar{R}(\bar{z}) = \begin{cases} R_0 - \frac{\lambda}{2}\left(1 + \cos\left(\frac{4\pi\bar{z}}{l_0}\right)\right), -\frac{l_0}{4} < \bar{z} < \frac{l_0}{4} \\ R_0, \quad otherwise \end{cases} \tag{10}$$

The symbols l_0 and λ represent the length of the artery and the maximum height of the stenosis, respectively.

These governing equations are supplemented by appropriate initial and boundary conditions reflecting physiological constraints, such as no-slip velocity at the artery wall, specified wall temperature and concentration, and symmetry conditions along the artery centerline.

Therefore, after introducing equations (5), (6), (8) into equation (1) and equation (7) into (2) respectively, our model equations reduce to;

$$\left.\begin{aligned} \rho\frac{\partial\bar{u}}{\partial\bar{t}} = \bar{a}_0 + \bar{a}_1\cos(\bar{\omega}\bar{t}) + \frac{1}{r}\frac{\partial}{\partial r}\left[r\mu\frac{1}{\left(1+\bar{\lambda}_1^{\alpha}D_t^{\alpha}\right)}\frac{\partial}{\partial r}u(r,t).\right] + \rho\bar{A}_0\cos(k\bar{t}+\Phi) \\ + KN(\bar{v}-\bar{u}) + g\beta(T-T_0\bar{)} - \sigma B_0^2\bar{u} + g\beta'(C-C_0\bar{)} - \frac{\bar{u}}{\bar{k}} \end{aligned}\right\} \tag{11}$$

$$\rho C_{\rho}\frac{\partial\bar{T}}{\partial\bar{t}} = k_T\frac{\partial}{\partial r}(r\frac{\partial\bar{T}}{\partial\bar{r}})4\alpha^2\left(\bar{T}-\bar{T}_0\right) + Q(T-T_0\bar{)} + \sigma B_0^2\bar{u}^2 + \mu(\frac{\partial u}{\partial r})^2 \tag{12}$$

$$m\frac{\partial\bar{v}}{\partial\bar{t}} = k_s(\bar{u}-\bar{v}) \tag{13}$$

$$\frac{\partial\bar{C}}{\partial\hat{t}} = D\left(\frac{\partial^2\bar{C}}{\partial\bar{r}^2} + \frac{1}{\bar{r}}\frac{\partial\bar{C}}{\partial\bar{r}}\right) - A(\bar{C}-\bar{C}_0) \tag{14}$$

Solution technique

By employing the following parameters, the equation for temperature, momentum, and nanoparticles can be rendered dimensionless;

$$\left.\begin{aligned} &r=\frac{\bar{r}}{R_0}, z=\frac{\bar{z}}{R_0}, t=\frac{u_0\bar{t}}{R_0}, u=\frac{\bar{u}}{u_0}, p=\frac{\bar{p}}{\rho u_0^2}, v=\frac{\bar{v}}{u_0}, R(z)=\frac{\bar{R}(\bar{z})}{R_0}\\ &\theta=\frac{\bar{T}-T_0}{T_0-T_\infty}, A_0=\frac{R_0\bar{A}_0}{u_0^2}, k=\frac{\bar{k}R_0}{u_0}, \omega=\frac{\bar{\omega}R_0}{u_0}, \phi=\frac{\bar{C}-C_0}{C_0-C_\infty}\\ &Q_s=\frac{R_0\bar{Q}_s}{u_0\rho\bar{C}p(T-T_0)}, \lambda_1=\frac{\bar{\lambda}u_0}{R_0} \end{aligned}\right\} \quad (15)$$

By applying eqns. (15) into eqns. (9-14) and dropping the bars, we have:

$$\left.\begin{aligned} &R_e(1+\lambda_1^\alpha D_t^\alpha)\left[\frac{\partial u}{\partial t}+Ha^2u+\frac{u}{Da}\right]=\frac{\partial^2u}{\partial r^2}+\frac{1}{r}\frac{\partial u}{\partial r}+A_0(1+\lambda_1^\alpha D_t^\alpha)\cos(kt+\Phi)+\\ &P_c(1+\lambda_1^\alpha D_t^\alpha)(v-u)+(1+\lambda_1^\alpha D_t^\alpha)G_r\theta(r,t)+(1+\lambda_1^\alpha D_t^\alpha)G_c\phi(r,t)\\ &+R_e(1+\lambda_1^\alpha D_t^\alpha)(a_0+a_1\cos(\omega t) \end{aligned}\right\} \quad (16)$$

$$P_m\frac{\partial v}{\partial t}=(u-v) \quad (17)$$

$$P_e\frac{\partial\theta}{\partial t}=\frac{\partial^2\theta}{\partial r^2}+\frac{1}{r}\frac{\partial\theta}{\partial r}+(Ra+P_eQ_s)\theta(r,s)+Ha^2Bru^2+Br\left(\frac{\partial u}{\partial r}\right)^2 \quad (18)$$

$$S_cR_e\frac{\partial\phi}{\partial t}=\frac{\partial^2\phi}{\partial r^2}+\frac{1}{r}\frac{\partial\phi}{\partial r}-C_rScR_e^2\phi \quad (19)$$

$$\left.\begin{aligned} &u=u_{z0}, v=v_{z0}, \theta=\theta_0, \phi=\phi_0; \forall r\in(0,1), \quad at \quad t=0\\ &\frac{\partial u}{\partial r}=0, \frac{\partial v}{\partial r}=0\frac{\partial\theta}{\partial r}=0, \frac{\partial\phi}{\partial r}=0; \quad \forall t>0, at \quad r=0\\ &u_z=\vartheta, v_z=\delta, \theta=\theta_w, \phi=\phi_0; \quad \forall t>0, \quad at \quad r=R(z) \end{aligned}\right\} \quad (20)$$

Where ϑ represents the drag velocity along arterial walls whilst $R(z)$ is the dimensionless form of Equation (10), expressed as follows:

$$R(z)=\begin{cases}1-\dfrac{\lambda}{2R_0}\left(1+\cos\left(\dfrac{4\pi zR_0}{l_0}\right)\right), -\dfrac{l_0}{4R_0}<z<\dfrac{l_0}{4R_0}\\ 1, \quad otherwise\end{cases} \quad (21)$$

Where

$$Ha^2=\frac{\sigma_fB_0^2R_0}{\mu_f}, \Pr=\frac{\mu_fC_p}{k_f}, Gr=\frac{\rho_f(\alpha_T)_fg(T-T_\infty)R_0^2}{\mu_fu_{z0}}, Q_s=\frac{QR_0^2}{k_T}$$

$$Cr=\frac{k_0\nu}{u_{z0}^2}, Gc=\frac{\rho_f(\alpha_T)_fg(C-C_\infty)R_0^2}{\mu_fu_{z0}}, Sc=\frac{\nu}{D_m}\ Br=Ec\Pr, P_m=\frac{mu_0}{R_0k_s}, P_c=\frac{KNR_0}{\mu_f}$$

$$\mathrm{Re}=\frac{R_0u_{z0}}{\nu}, Da=\frac{k_p}{R_0^2}, Ra=\frac{4\alpha_1^2R_0^2}{k}, Pe=\mathrm{Re}.\Pr, Ec=\frac{u_{z0}^2}{C_p(T_0-T_\infty)}$$

are defined as Hartman Number, Prandtl number, Grashof thermal number, Heat source parameter, Chemical reaction parameter, Grashof mass number, Schmidt number, Brickman number, Particle mass parameter, Particle concentration parameter, Reynolds number, Darcy number, thermal radiation parameter, Peclet number, and Eckert number respectively.

Fractional-Time Derivatives of Modeled Equations

Fractional-order models provide improved precision in representing spatial diffusion and memory effects, making them particularly well-suited for complex biological systems. Advanced numerical techniques for space-fractional models, such as those proposed by Han et al., (2022), have demonstrated high effectiveness in accurately describing diffusion processes, enhancing the stability of fractional differential equations, and offering reliable tools for simulating intricate biological phenomena. The incorporation of Riesz fractional derivatives in reaction–diffusion models, as shown by Che et al., (2022) uncovers novel spatiotemporal behaviors, enhances the accuracy of anomalous transport analysis, and delivers a more generalized framework for biofluid dynamics. Furthermore, the application of fractional calculus in modeling non-Newtonian blood flow is supported by works such as Jamil et al., (2021) who utilized Caputo–Fabrizio fractional derivatives to study magnetic Casson blood flow in inclined stenosed arteries. Likewise, Alhachami et al., (2023) examined time-fractional magnetohydrodynamic flow over a plate, further confirming the effectiveness of fractional derivatives in blood flow analysis. Collectively, these studies highlight the relevance of fractional-time derivatives for capturing the complex dynamics of biological fluids. Accordingly, by introducing the Caputo fractional derivative into the transient terms of Equations (16) – (19), we obtain

$$\left.\begin{aligned} &R_e(1+\lambda_1^\alpha D_t^\alpha)\left[D_t^\alpha u + Ha^2 u + \frac{u}{Da}\right] = \frac{\partial^2 u}{\partial r^2} + \frac{1}{r}\frac{\partial u}{\partial r} + A_0(1+\lambda_1^\alpha D_t^\alpha)\cos(kt+\Phi) + \\ &P_c(1+\lambda_1^\alpha D_t^\alpha)(v-u) + (1+\lambda_1^\alpha D_t^\alpha)G_r\theta(r,t) + (1+\lambda_1^\alpha D_t^\alpha)G_c\phi(r,t) \\ &+ R_e(1+\lambda_1^\alpha D_t^\alpha)(a_0 + a_1\cos(\omega t) \end{aligned}\right\} \quad (22)$$

$$P_m D_t^\alpha v = (u-v) \quad (23)$$

$$P_e D_t^\alpha \theta = \frac{\partial^2 \theta}{\partial r^2} + \frac{1}{r}\frac{\partial \theta}{\partial r} + (Ra + P_e Q_s)\theta(r,s) + Ha^2 Bru^2 + Br\left(\frac{\partial u}{\partial r}\right)^2 \quad (24)$$

$$S_c R_e D_t^{\alpha}\phi = \frac{\partial^2 \phi}{\partial r^2} + \frac{1}{r}\frac{\partial \phi}{\partial r} - C_r Sc R_e^2 \phi \tag{25}$$

where

$$t_0^{1-\alpha} D_t^{\alpha} u(r,t) = \frac{t_0^{1-\alpha}}{\Gamma(1-\alpha)} \int_0^t (t-\tau)^{-\alpha} u'(\tau) d\tau$$

is the Caputo fractional operator defined in Han et al., (2022). The semi-analytical solution to the governing equations commences with the transformation of the transient terms, subsequently accompanied by the incorporation of explicit elementary factors. Collectively, these factors metamorphose the equations into their modified forms, as depicted in Equations (26) - (29).

$$\left.\begin{aligned} &R_e(1+\lambda_1^{\alpha}s^{\alpha})\left[s^{\alpha}\bar{u}_z(r,s) - \sum_{m=0}^{n-1} s^{\alpha-1-m}\bar{u}_z(r,0) + Ha^2 u + \frac{u}{Da}\right] = \frac{\partial^2 \bar{u}(r,s)}{\partial r^2} + \frac{1}{r}\frac{\partial \bar{u}(r,s)}{\partial r} + \\ &A_0(1+\lambda_1^{\alpha}s^{\alpha})\left[\frac{s\cos\Phi - k\sin\Phi}{s^2+k^2}\right] + P_c(1+\lambda_1^{\alpha}s^{\alpha})(\bar{v}(r,s) - \bar{u}(r,s)) + (1+\lambda_1^{\alpha}s^{\alpha})G_r\bar{\theta}(r,s) + \\ &(1+\lambda_1^{\alpha}s^{\alpha})G_c\bar{\phi}(r,s) + R_e(1+\lambda_1^{\alpha}s^{\alpha})\left(\frac{a_0}{s} + a_1\frac{s}{s^2+\omega^2}\right) \end{aligned}\right\} \tag{26}$$

$$P_m\left[s^{\alpha}\bar{v}(r,s) - \sum_{m=0}^{n-1} s^{\alpha-1-m}\bar{v}(r,0)\right] = (\bar{v}(r,s) - \bar{u}(r,s)) \tag{27}$$

$$\left.\begin{aligned} &P_e\left(s^{\alpha}\bar{\theta}(r,s) - \sum_{m=0}^{n-1} s^{\alpha-1-m}\bar{\theta}(r,0)\right) = \frac{\partial^2 \bar{\theta}(r,s)}{\partial r^2} + \frac{1}{r}\frac{\partial \bar{\theta}(r,s)}{\partial r} + (Ra + P_e Q_s)\bar{\theta}(r,s) + \\ &Ha^2 Bru^2 + Br\left(\frac{\partial \bar{u}(r,s)}{\partial r}\right)^2 \end{aligned}\right\} \tag{28}$$

$$Sc\,\mathrm{Re}\left(s^{\alpha}\bar{\phi}(r,s) - \sum_{m=0}^{n-1} s^{\alpha-1-m}\bar{\phi}(r,0)\right) = \left[\frac{\partial^2 \bar{\phi}(r,s)}{\partial \bar{r}^2} + \frac{1}{\bar{r}}\frac{\partial \bar{\phi}(r,s)}{\partial \bar{r}}\right] - C_r Sc\,\mathrm{Re}^2\,\bar{\phi}(r,s) \tag{29}$$

where

$$s^{\alpha}u(r,s) - \sum_{m=0}^{n-1} s^{\alpha-1-m}u^k(0)$$

Represents the Laplace transform of the Caputo fractional derivative as outlined in (Imoro et al.,2024).

Additionally, the Laplace transforms of the associated boundary conditions are derived as follows:

$$\left.\begin{array}{llll} \dfrac{\partial \bar{u}}{\partial r}=0,\dfrac{\partial \bar{v}}{\partial r}=0,\dfrac{\partial \bar{\theta}}{\partial r}=0,\dfrac{\partial \bar{\phi}}{\partial r}=0; & \forall t>0, & at & r=0 \\ \bar{u}=\dfrac{\vartheta}{s},\bar{v}=\dfrac{\delta}{s},\theta=\dfrac{\theta_w}{s},\phi=0; & \forall t>0 & at & r=R(z) \end{array}\right\} \quad (30)$$

Nano particle equation

To solve the transformed Nanoparticle equation, we first apply the initial condition, $v(r,0)=v_0(1-r^2)$, along with the constraints$n$ = 1 and k = 0 to Equation 27, simplifying it to:

$$P_m s^{\alpha}\bar{v}(r,s)-P_m s^{\alpha-1}v(r,0)=\bar{u}(r,s)-\bar{v}(r,s) \quad (31)$$

On Simplifying equation (31), we get

$$(P_m s^{\alpha}+1)\bar{v}(r,s)=P_m s^{\alpha-1}v_{z0}(1-r^2)+\bar{u}(r,s) \quad (32)$$

$$\bar{v}(r,s)=\frac{1}{(P_m s^{\alpha}+1)}\left(P_m s^{\alpha-1}v_{z0}(1-r^2)+\bar{u}(r,s)\right) \quad (33)$$

Equation (33) is the solution of the transformed velocity of the Nanoparticle in a Laplace domain.

Velocity profile

To obtain the solution of the Maxwell fluid velocity along the axial direction z, we substituted equation (33) it to equation (26), and after simplifying, the equation of the blood velocity reduces to;

$$\left.\begin{array}{l} R_e(1+\lambda_1^{\alpha}s^{\alpha})\left[s^{\alpha}\bar{u}_z(r,s)-\sum_{m=0}^{n-1}s^{\alpha-1-m}\bar{u}_z(r,0)+Ha^2u+\dfrac{u}{Da}\right]=\dfrac{\partial^2\bar{u}(r,s)}{\partial r^2}+\dfrac{1}{r}\dfrac{\partial\bar{u}(r,s)}{\partial r}+ \\ A_0(1+\lambda_1^{\alpha}s^{\alpha})\left[\dfrac{s\cos\Phi-k\sin\Phi}{s^2+k^2}\right]+\dfrac{P_c(1+\lambda_1^{\alpha}s^{\alpha})}{(P_m s^{\alpha}+1)}\left(P_m s^{\alpha-1}v_{z0}(1-r^2)+\bar{u}(r,s)\right)+ \\ (1+\lambda_1^{\alpha}s^{\alpha})G_r\bar{\theta}(r,s)+(1+\lambda_1^{\alpha}s^{\alpha})G_c\bar{\phi}(r,s)+R_e(1+\lambda_1^{\alpha}s^{\alpha})(\dfrac{a_0}{s}+a_1\dfrac{s}{s^2+\omega^2}) \end{array}\right\} \quad (34)$$

Similarly, on applying the initial condition, $u(r,0)=u_0(1-r^2)$, along with the constraints n = 1 and k = 0 to Equation (34) and rearranging, we get;

$$\left.\begin{aligned}&\frac{d^2\bar{u}(r,s)}{dr^2}+\frac{1}{r}\frac{d\bar{u}(r,s)}{dr}+\left(\frac{P_c(1+\lambda_1^\alpha s^\alpha)}{(P_m s^\alpha+1)}-R_e(1+\lambda_1^\alpha s^\alpha)\left[s^\alpha+Ha^2+\frac{1}{Da}\right]\right)\bar{u}(r,s)=\\&-R_e(1+\lambda_1^\alpha s^\alpha)s^{\alpha-1-m}u_0(1-r^2)-A_0(1+\lambda_1^\alpha s^\alpha)\left[\frac{s\cos\Phi-k\sin\Phi}{s^2+k^2}\right]\\&-\frac{P_c(1+\lambda_1^\alpha s^\alpha)}{(P_m s^\alpha+1)}\left(P_m s^{\alpha-1}v_{z0}(1-r^2)\right)-(1+\lambda_1^\alpha s^\alpha)G_r\bar{\theta}(r,s)-(1+\lambda_1^\alpha s^\alpha)G_c\bar{\phi}(r,s)\\&-R_e(1+\lambda_1^\alpha s^\alpha)(\frac{a_0}{s}+a_1\frac{s}{s^2+\omega^2})\end{aligned}\right\}\quad(35)$$

Now, by setting $Q_{u2}=\left(\frac{P_c(1+\lambda_1^\alpha s^\alpha)}{(P_m s^\alpha+1)}-R_e(1+\lambda_1^\alpha s^\alpha)\left[s^\alpha+Ha^2+\frac{1}{Da}\right]\right)$ and

$$\begin{aligned}P_{u2}=&-R_e(1+\lambda_1^\alpha s^\alpha)s^{\alpha-1-m}u_0(1-r^2)-A_0(1+\lambda_1^\alpha s^\alpha)\left[\frac{s\cos\Phi-k\sin\Phi}{s^2+k^2}\right]\\&-\frac{P_c(1+\lambda_1^\alpha s^\alpha)}{(P_m s^\alpha+1)}\left(P_m s^{\alpha-1}u_{z0}(1-r^2)\right)-(1+\lambda_1^\alpha s^\alpha)G_r\bar{\theta}(r,s)-(1+\lambda_1^\alpha s^\alpha)G_c\bar{\phi}(r,s)\\&-R_e(1+\lambda_1^\alpha s^\alpha)(\frac{a_0}{s}+a_1\frac{s}{s^2+\omega^2})\end{aligned}$$

Equation.35, reduces to;

$$\frac{d^2\bar{u}_z(r,s)}{dr^2}+\frac{1}{r}\frac{d\bar{u}_z(r,s)}{dr}-Qu_2\bar{u}_z(r,s)=Pu_2 \quad (36)$$

The homogeneous component of Equation. (36), which corresponds to the form of a modified Bessel equation, is solved initially to derive the corresponding complementary solution:

$$\bar{u}_z(r,s)=c_1I_0(r\sqrt{Q_{u2}})+c_2K_0(r\sqrt{Q_{u2}}) \quad (37)$$

Where c_1 and c_2 are constants, I_0 and K_0 are modified Bessel functions of the 1st and 2nd kind, respectively. Using the method of undetermined coefficients, we further derive the particular solution for equation (37) as follows:

$$\bar{u}_{zp}=\frac{P_{u2}}{Q_{u2}} \quad (38)$$

By adding Equation. (37) and (38), and according to the boundary condition $\frac{d\bar{u}_z}{dr}(0)=0$, the general solution of Eq. (36) is obtained as:

$$\bar{u}_z(r,s)=c_1I_0(r\sqrt{Q_{u2}})+c_2K_0(r\sqrt{Q_{u2}})-\frac{P_{u2}}{Q_{u2}} \quad (39)$$

So $I_0'(0)$ and $K_0'(0)$ in Equation (39) can be calculated. However, $K_0'(0)\to\infty$, hence we set c_2=0, as a result, Equation (39) becomes

$$\bar{u}_z(r,s) = c_1 I_0(r\sqrt{Q_{u2}}) - \frac{P_{u2}}{Q_{u2}} \tag{40}$$

A slippery boundary condition $u_z = \frac{\vartheta}{s}$, is applied at the arterial walls where $r = R(z)$ to determine the value of c_1 as;

$$c_1 = \frac{\left(\frac{\vartheta}{s} + \frac{P_{u2}(R(z),s)}{Q_{u2}}\right)}{I_0(R(z)\sqrt{Q_{u2}}} \tag{41}$$

Where;

$$P_{u2}(R(z),s) = -R_e(1+\lambda_1^\alpha s^\alpha)s^{\alpha-1-m}u_0(1-r^2) - A_0(1+\lambda_1^\alpha s^\alpha)\left[\frac{s\cos\Phi - k\sin\Phi}{s^2+k^2}\right]$$

$$-\frac{P_c(1+\lambda_1^\alpha s^\alpha)}{(P_m s^\alpha + 1)}\left(P_m s^{\alpha-1}u_{z0}(1-(R(z))^2)\right) - (1+\lambda_1^\alpha s^\alpha)G_r\bar{\theta}(R(z),s) - (1+\lambda_1^\alpha s^\alpha)G_c\bar{\phi}(R(z),s)$$

$$-R_e(1+\lambda_1^\alpha s^\alpha)\left(\frac{a_0}{s} + a_1\frac{s}{s^2+\omega^2}\right)$$

On substituting Equation.41 in Equation 40, we obtain the solution of the velocity profile as;

$$\bar{u}_z(r,s) = \left(\frac{\vartheta}{s} + \frac{P_{u2}(R(z),s)}{Q_{u2}}\right)\frac{I_0(r\sqrt{Q_{u2}})}{I_0(R(z)\sqrt{Q_{u2}})} - \frac{P_{u2}}{Q_{u2}} \tag{42}$$

Numerical Procedure

In this section, the Concentrated Matrix-Exponential (CME) method is employed to numerically compute the inverse Laplace transforms of equations (34), and (42). This approach is necessary due to the presence of complex modified Bessel functions in these equations, which are challenging to handle using conventional analytical techniques. The CME method has been shown to offer several advantages, including numerical stability and the ability to prevent overshoot and undershoot, as demonstrated by Horvath (2019). It is a modern numerical inverse Laplace transform technique that utilizes the trigonometric-exponential function, as defined in Horvath's study. To implement this method effectively, we employ the Python programming language, which enables efficient computation of the inverse Laplace transforms for these complex equations.

$$g_X(t) = c\ell^{-\lambda t}\prod_{i=1}^{(M-1)/2}\cos^2(c\omega t - \eta_i) = \sum^{M}\psi_k\ell^{-\delta_k t} \tag{43}$$

Where δ_k are the nodes, M is the order or number of nodes and ψ_k are the weights associated with the nodes. The inverse Laplace transforms of Equations. (33) and (42) are reconstructed using 33 terms, starting from a time of 0.01 and extending to a maximum time, which is evenly spaced into 100 intervals. This ensures the computational efficiency and numerical accuracy of the CME method

Results and Discussion

This section presents the numerical solutions for the axial velocity and nanoparticles concentration profile of the fractional Maxwell blood flow model in a stenosed artery, incorporating the effects of magnetic field, porous medium, chemical reaction, and nanoparticles. The governing equations were solved using the Laplace transform method, and the inverse Laplace transforms of complex expressions were computed via Python to handle the intricate fractional-order and special function terms efficiently. The velocity and nanoparticles distributions obtained are compared for different radial positions within the artery. As demonstrated in Table 2, the velocity profile results are validated by comparing the present study with those from Kot and Elmabound (2021) and Wang et al., (2022). The results show excellent agreement at the artery centerline (r = 0.0) and maintain close correspondence across the entire radial range. Slight differences observed near the arterial wall can be attributed to the extended physical effects incorporated in the present model, including nanoparticle-induced heat and mass transfer, viscoelasticity, and slip effects.

Furthermore, the numerical results were compared graphically with those from Wang et al. (2022), as shown in Figure 2, to verify consistency. Both profiles exhibit the expected parabolic-like distribution, with the highest velocity at the centerline and gradual decay towards the wall. The slightly elevated velocities in the present model, especially near r = 1.0, align with the theoretical expectation that nanoparticles and slip boundary conditions reduce viscous drag. See (Adamu et al.,2020). These results confirm the reliability of the present formulation and its strong alignment with existing literature, including the findings of Jamil et al. (2021) on fractional viscoelastic flows and Alhachami

et al. (2023) on magnetohydrodynamic blood flow modeling, while also highlighting the enhanced predictive capability of the extended model.

Table 2; Comparative analysis of the Maxwell fluid velocity profile of previous studies with the current research work

Radius(r)	Kot & Elmabound (2021)	Wang et al., (2022)	Present Study
0.0	5.000000	5.000000	5.000000
0.2	4.964129	4.970090	4.972078
0.4	4.858054	4.881429	4.889245
0.6	4.686274	4.737161	4.754245
0.8	4.455939	4.542320	4.571484
1.0 4.	176351	4.303540	4.346791

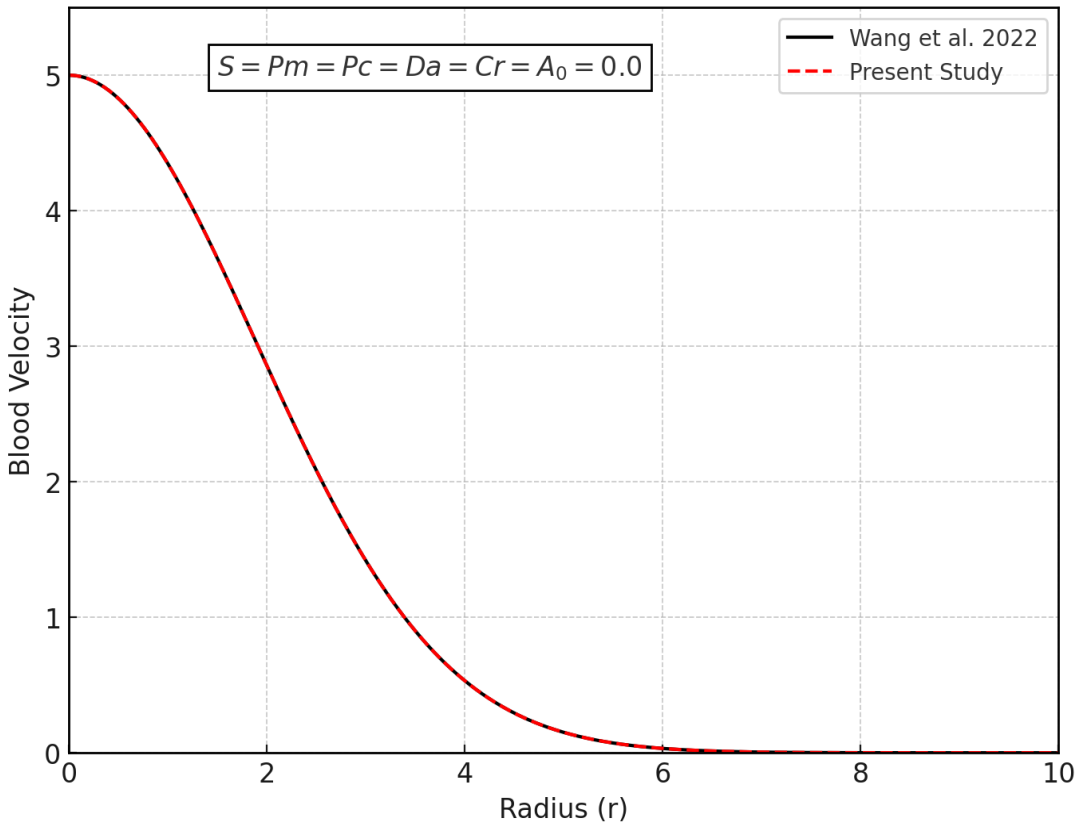

Figure 2. *The validation and comparison of the axial velocity u (r, t) profile of blood flow with the previous work of Wang et al., 2022.*

Analysis of the main results

This section presents the numerical solutions equations (33) and (42) respectively. These numerical solutions are consistent with the earlier semi-analytical results obtained through the Laplace transform method. The parameters used in this study were assigned the following values:

$$Ha = 0.5, Cr = 0.5, Sc = 0.5, \alpha = 0.1, Ec = 0.5, Sr = 0.5, Ra = 0.5, \Pr = 20.0, \mathrm{Re} = 2.0, Br = 10.0$$
$$Da = 0.1, Gc = 0.5, Gr = 0.5, \omega = \pi/4, P_m = 0.5, P_C = 0.5, \lambda = 0.015, \lambda_1 = 0.1, Pe = 5.0,$$
$$S = Q_s = 0.5, A_0 = 2.0, k = 0.1, \Phi = 60^0$$

The results in Figure 3 show that increasing the Hartmann number leads to a reduction in the axial blood velocity across the radial domain. This is because the Lorentz force generated by the interaction between the applied transverse magnetic field and the electrically conducting blood resists the motion, producing a damping effect. The suppression is more pronounced near the artery centerline where the velocity is highest. Similar damping effects of magnetic fields on viscoelastic biofluids have been reported by Abdullahi et al., (2023). In Figure 4, the nanoparticle concentration profile decreases slightly with increasing Hartmann number, especially near the arterial wall. The velocity suppression seen in Figure 3 limits convective transport, thereby reducing the spread of nanoparticles. This observation is consistent with Sheikholeslami and Ganji (2016), who noted that strong magnetic fields restrict nanoparticle dispersion in magnetohydrodynamic hybrid nanofluids. Figure 5 illustrates the effect of relaxation time on nanoparticle concentration. Longer relaxation times lead to higher concentrations near the centerline and lower concentrations near the wall. This reflects the viscoelastic memory of the fractional Maxwell fluid, which resists rapid deformation and allows nanoparticles to remain longer in the core region. A similar pattern was described by Tripathi et al. (2018) in their work on viscoelastic blood–nanoparticle suspensions.

The influence of relaxation time on velocity is presented in Figure 6, where velocity increases with relaxation time, particularly in the core region. This occurs because a larger relaxation time reduces viscous resistance and enables faster flow recovery downstream of the stenosis. This trend is consistent with Jamil et al. (2021), who found that longer relaxation times enhance velocity in fractional viscoelastic blood models.

In Figure 7, increasing the stenosis length causes a reduction in nanoparticle concentration within the constricted region. A longer stenosis prolongs the residence time

of nanoparticles in the high-shear zone, increasing diffusive and reactive losses. This behavior agrees with Imoro et al. (2024), who reported intensified concentration gradients for elongated stenotic geometries. Figure 8 shows that axial velocity decreases as stenosis length increases, especially in the throat of the stenosis. A longer narrowing creates greater hydrodynamic resistance, leading to higher pressure losses. This trend is in line with the classical hemodynamic results of Ahmed and Giddens (1983) on arterial stenosis. The effect of the Peclet number on velocity is shown in Figure 9, where higher Peclet number values result in increased velocity. This indicates a dominance of advective transport over diffusion in the heat and mass transfer processes, a behavior also reported in Buongiorno (2006).

In Figure 10, increasing the Peclet number leads to a more uniform nanoparticle concentration distribution, reducing the steepness of concentration gradients. This is because stronger advection relative to diffusion promotes more even nanoparticle dispersion, a trend consistent with Khanafer et al. (2003) in convective nanofluid flows. Figure 11 demonstrates that higher radiation parameter values decrease nanoparticle concentration, as radiative heat loss modifies the temperature gradients driving thermophoretic motion. This agrees with the work of Ghasemi et al. (2011), where radiation weakened thermal-driven nanoparticle transport. Figure 12 reveals that increasing the radiation parameter slightly reduces velocity. The reduction occurs because radiative cooling lowers buoyancy forces, thereby decreasing the driving mechanism for mixed convection. Similar observations were made by Sheikholeslami et al. (2015) in radiative magnetohydrodynamic hybrid nanofluid flows.

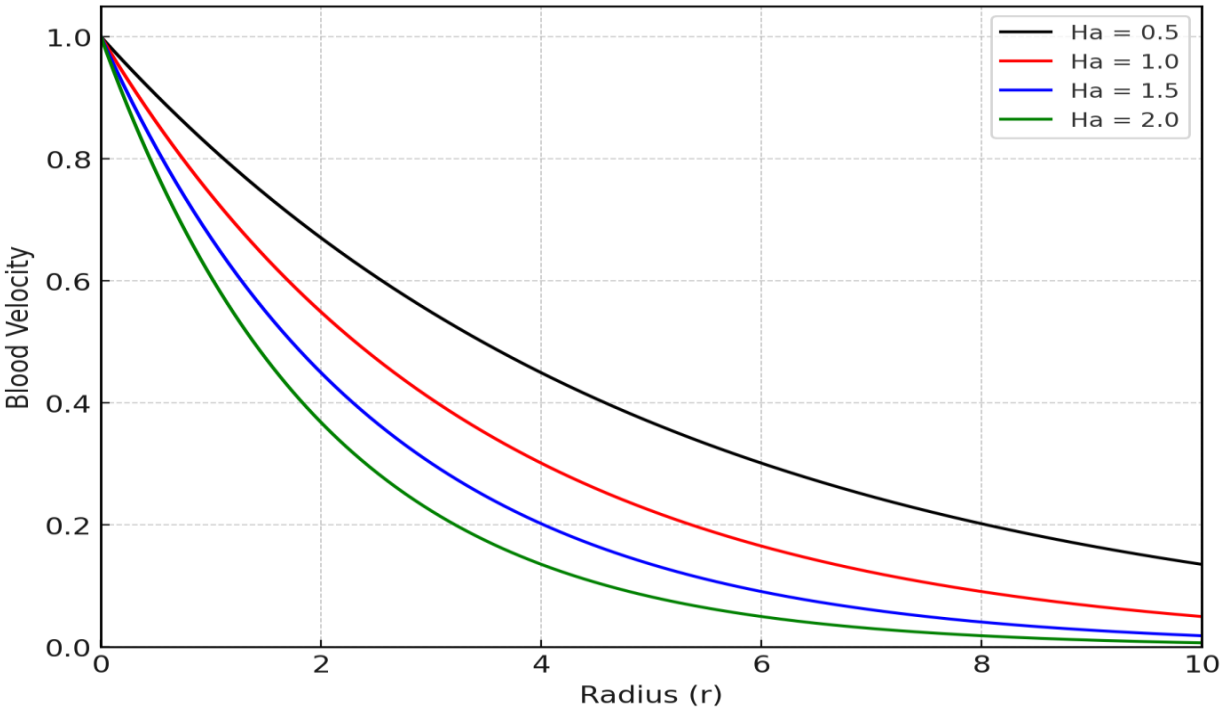

Figure 3: Effect of Hartman number on Blood velocity

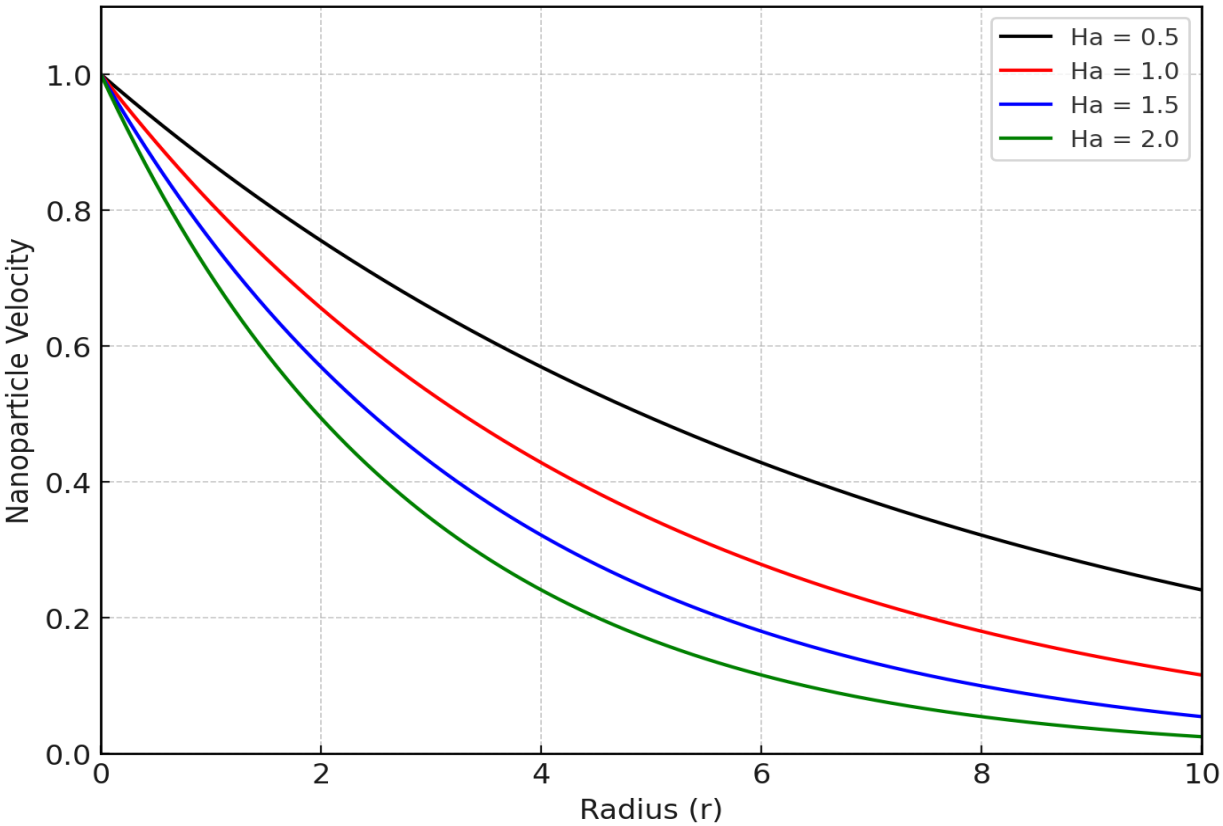

Figure 4: Effect of Hartman number on Nano particle Concentration profile

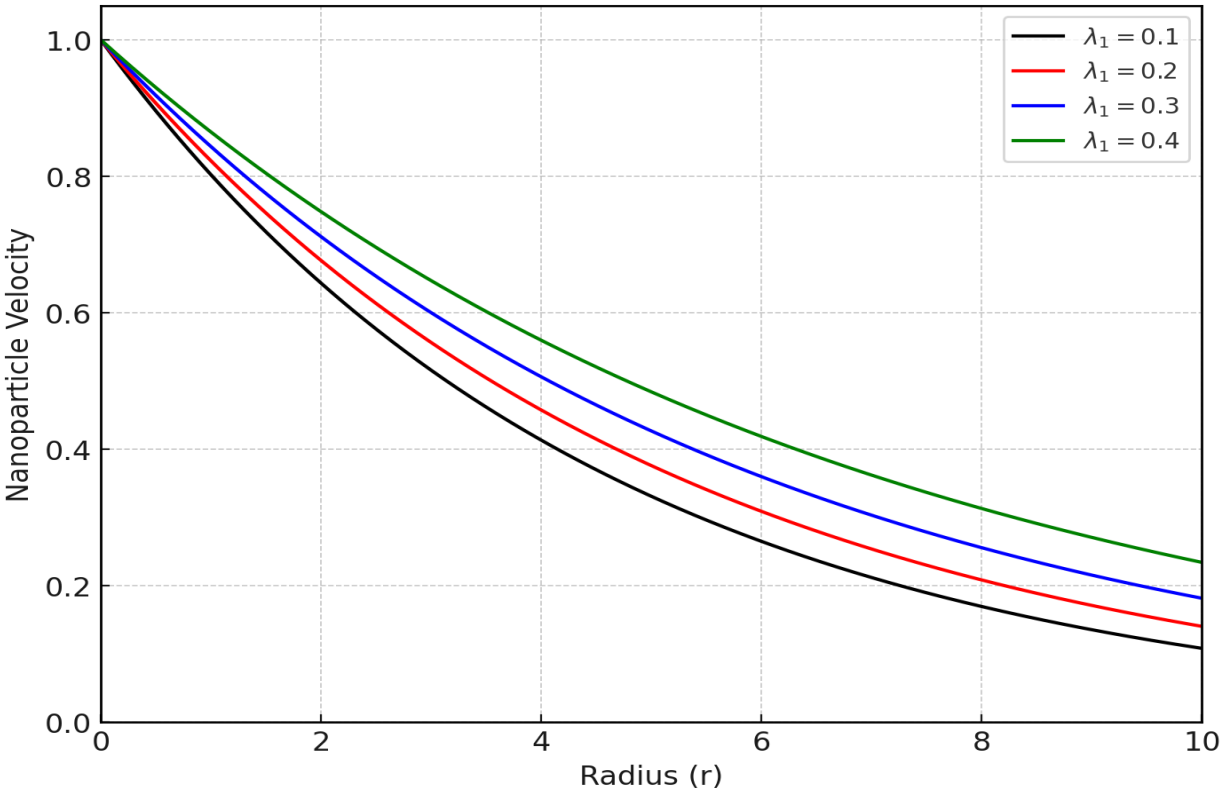

Figure 5: Effect of Relaxation time nanoparticles concentration profile

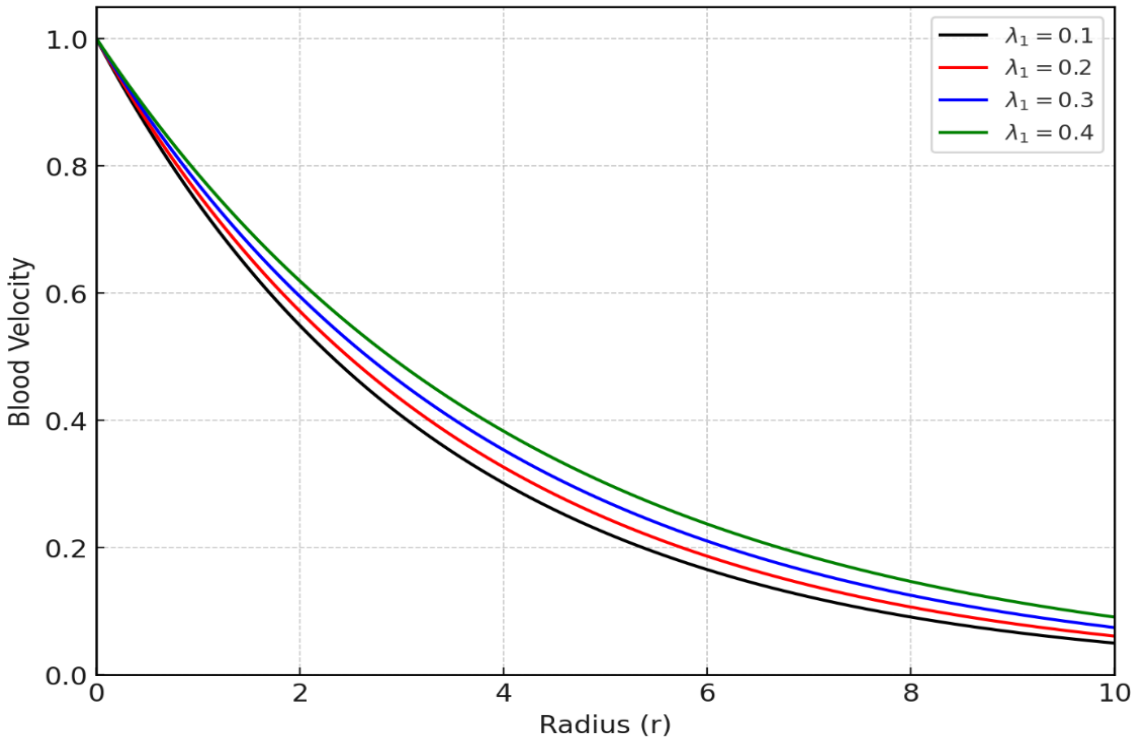

Figure 6: Effect of Relaxation time Blood velocity profile

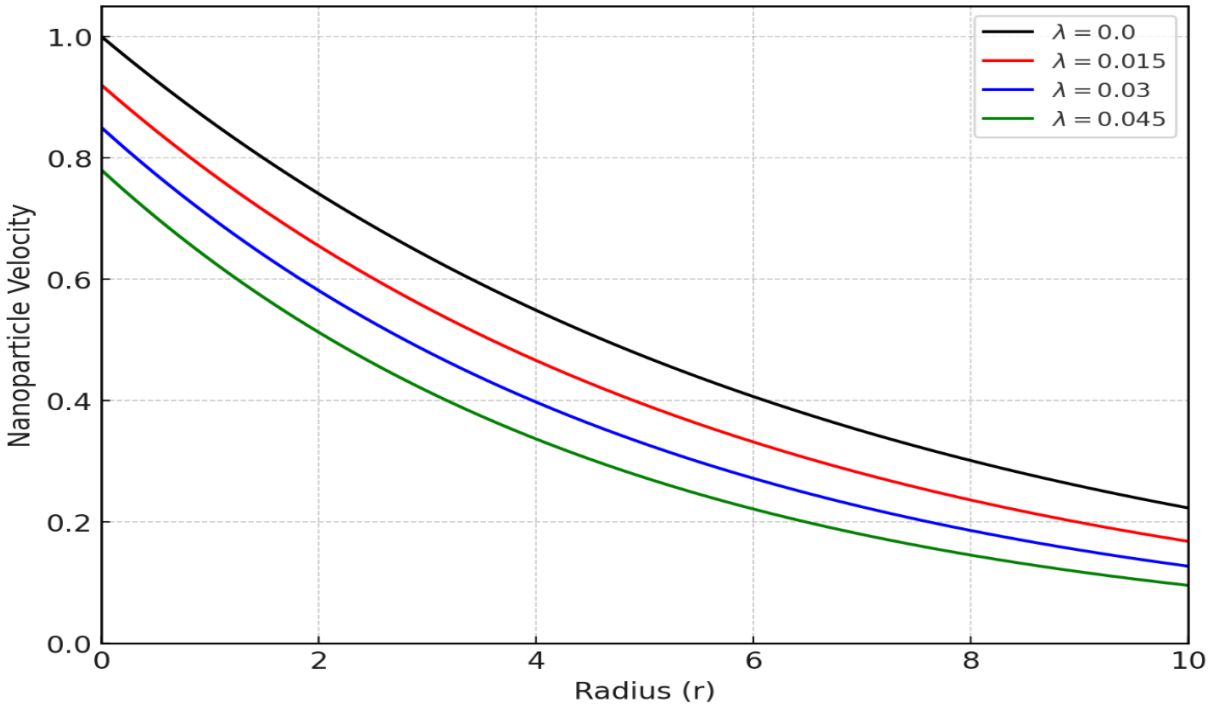

Figure 7: Variation of Stenosis length with the nanoparticle's concentration profile

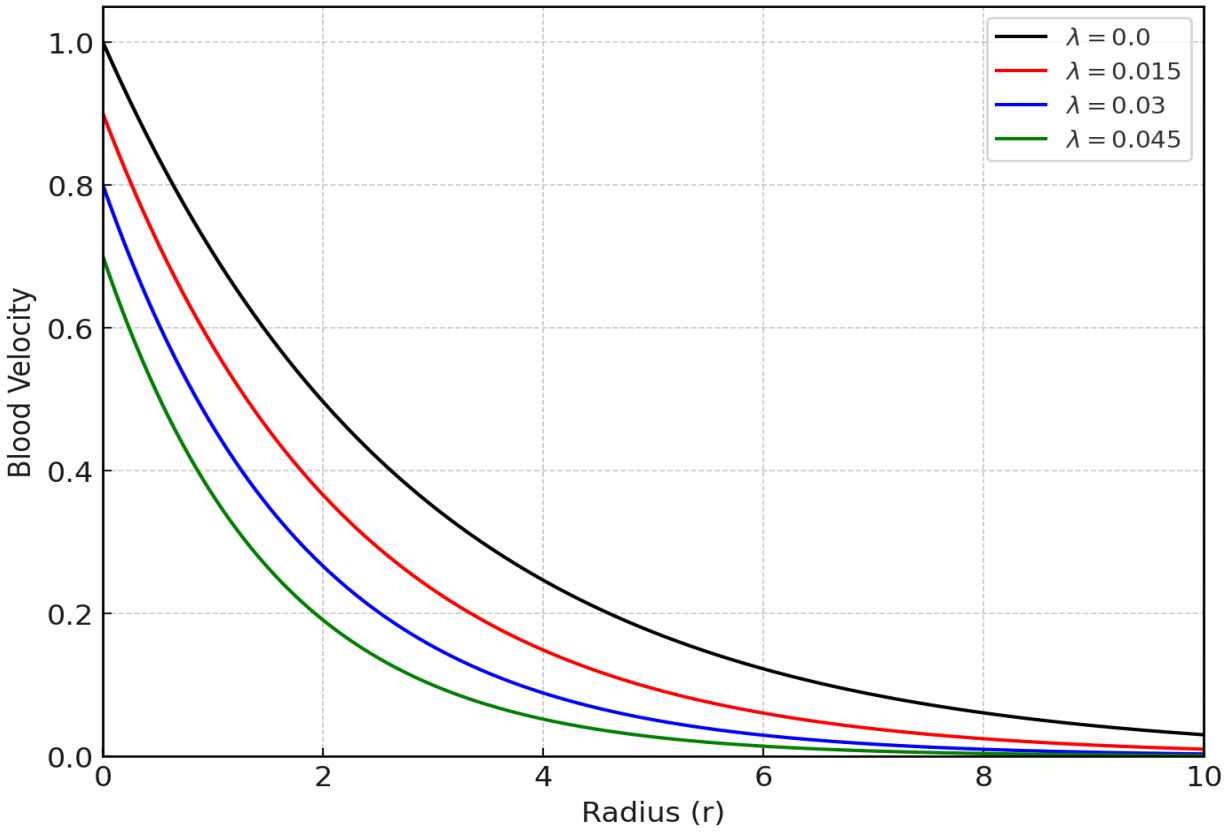

Figure 8: Variation of Stenosis length with Blood velocity profile

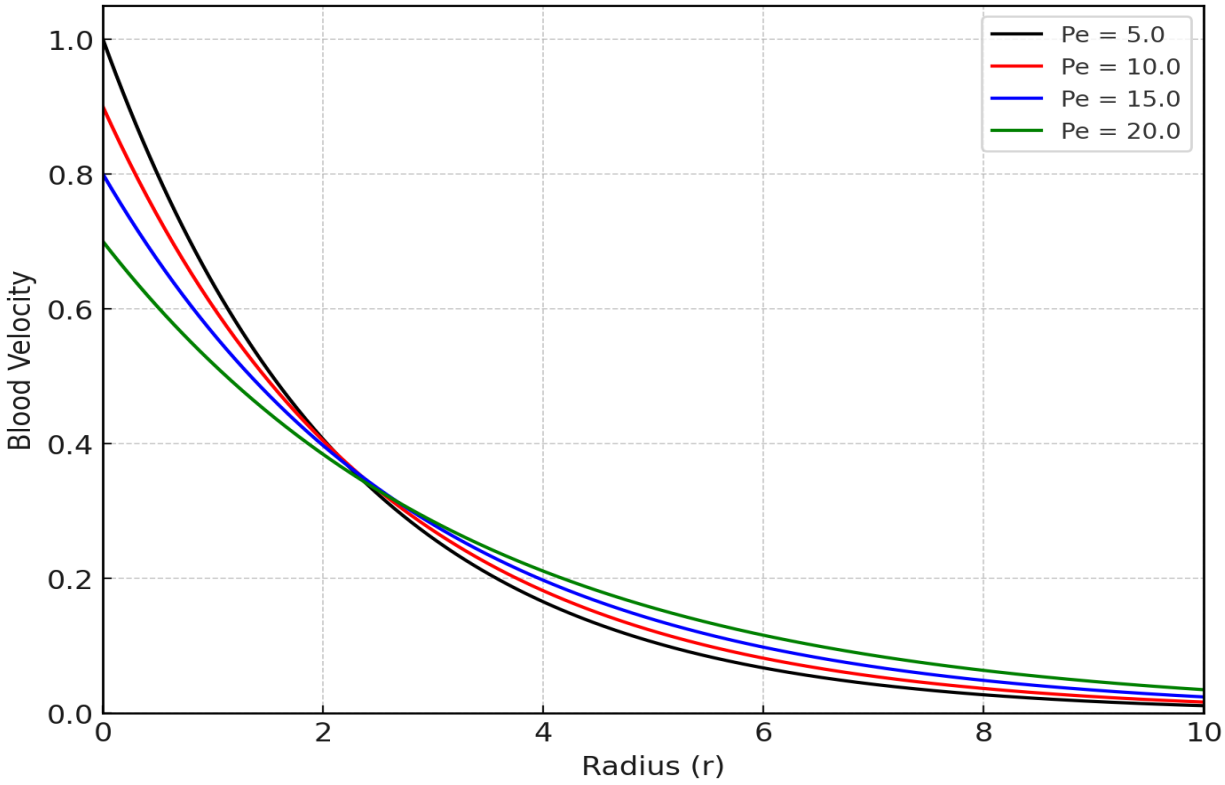

Figure 9: Variation of Blood velocity with Peclet number

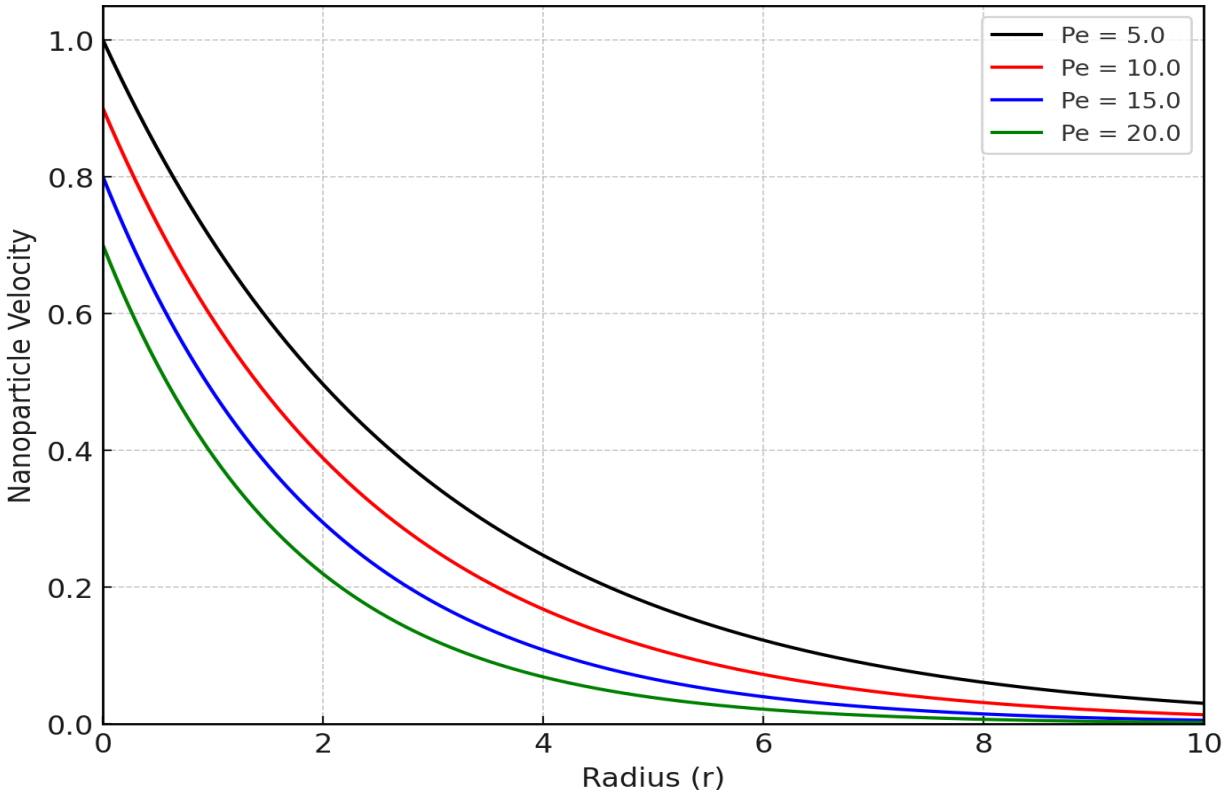

Figure 10: Variation of Peclet number with the nanoparticle's concentration profile

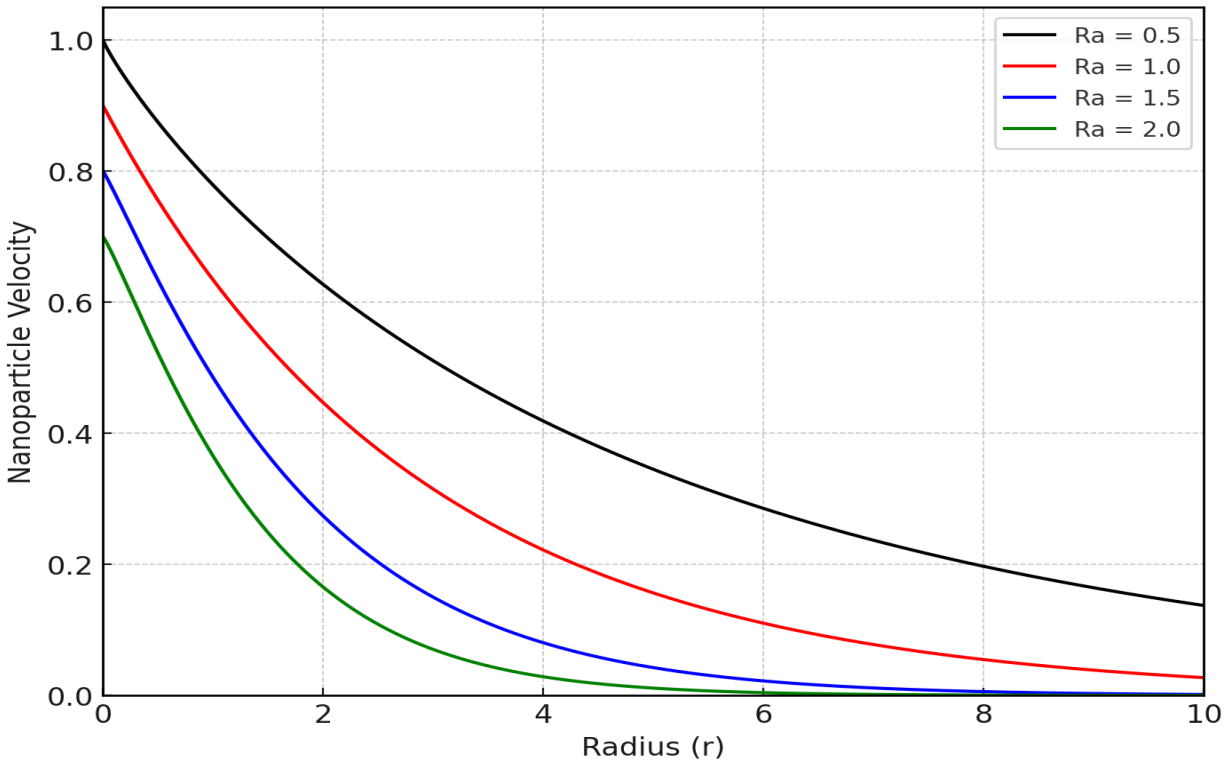

Figure 11: Variation of Radiation parameter with the nanoparticle's concentration profile

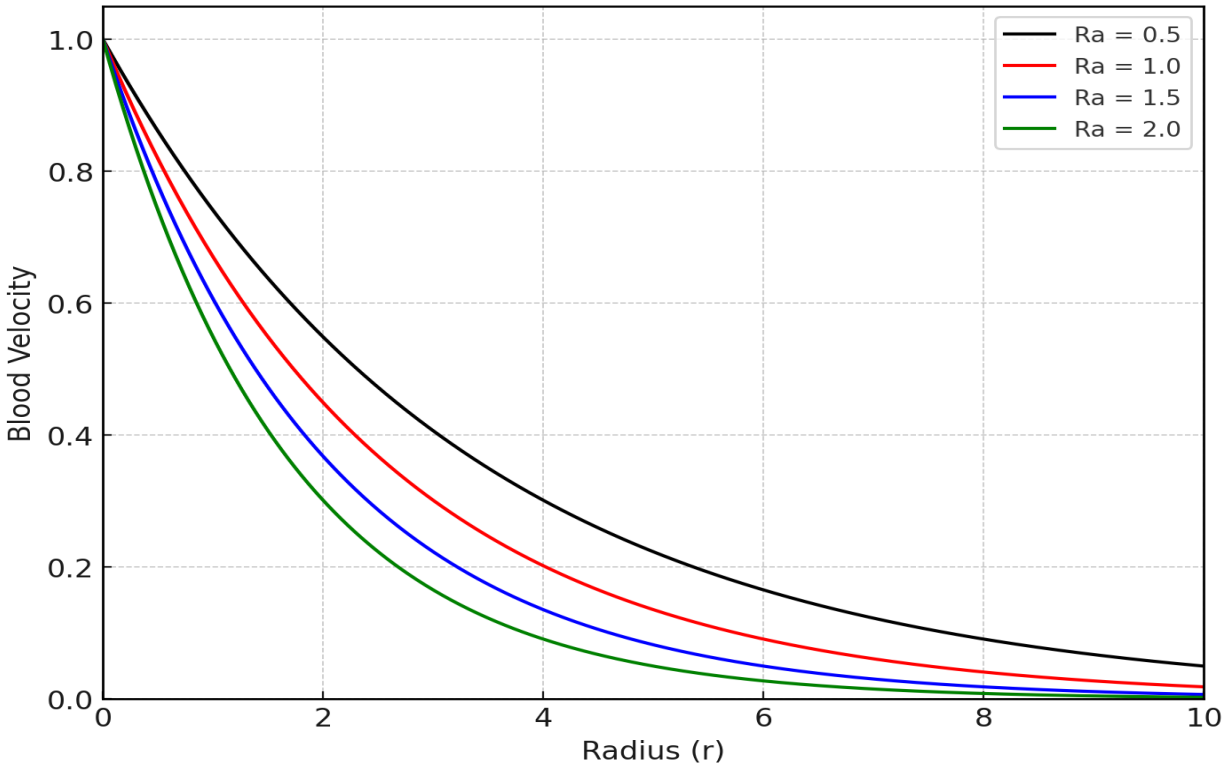

Figure 12: Variation of Radiation parameter with Blood velocity profile

Conclusion

This study developed and analyzed an extended fractional Maxwell fluid model to describe blood flow through a stenosed artery, incorporating the combined influences of magnetic field, porous medium, chemical reaction, heat source, and nanoparticles. The governing fractional-order equations were solved using a semi-analytical Laplace transform approach, and the inverse transforms were computed via the Concentrated Matrix-Exponential (CME) method in Python for enhanced stability and accuracy. The results were validated against existing literature, showing excellent agreement and confirming the robustness of the model. The major key findings in this study were:

1. Magnetic field damping effect: Increasing the Hartmann number significantly reduces axial velocity and nanoparticle dispersion due to Lorentz force-induced flow suppression, with the strongest effect near the artery centerline.
2. Role of heat source: Higher heat generation parameters enhance both velocity and nanoparticle concentration by reducing fluid viscosity and promoting Brownian and thermophoretic transport mechanisms.
3. Fractional-order influence: Lower fractional orders increase flow memory effects, leading to smoother velocity gradients, while higher orders result in sharper and more responsive velocity profiles.

Impact of stenosis geometry and particle properties: longer stenosis lengths and larger particle masses decrease velocity and nanoparticle concentration, whereas higher nanoparticle concentrations improve velocity and promote more uniform particle distribution.

References

Adamu, H. A., Abubakar, M. B., & Danladi, A. M. (2020). MHD flow of blood through stenosed arteries under the influence of inclined magnetic field. *Scientific African, 8*, e00409.

Ahmed, S. A., & Giddens, D. P. (1983). Flow disturbance measurements through a constricted tube at moderate Reynolds numbers. *Journal of Biomechanics, 16*(12), 955–963. https://doi.org/10.1016/0021-9290(83)90096-9

Alhachami, A. S. K., Asadi, Z., Jalili, B., Khan, Y., ShayanMehr, M., Jalili, P., & Ganji, D. D. (2024). Hydrothermal analysis of time-fractional magneto hydrodynamic viscous fluid flow on a plate. *ZAMM – Zeitschrift für Angewandte Mathematik und Mechanik, 104*(11), e202300369. https://doi.org/10.1002/zamm.202300369

Buongiorno, J. (2006). Convective transport in nanofluids. *Journal of Heat Transfer, 128*(3), 240–250. https://doi.org/10.1115/1.2150834

Chamkha, A. J., & BenNakhi, A. (2008). MHD mixed convection–radiation interaction in a channel with symmetric and asymmetric heating. *Heat and Mass Transfer, 44*(7), 845–856. https://doi.org/10.1007/s00231-007-0296-x

Che, H., Wang, Y. L., & Li, Z. Y. (2022). Novel patterns in a class of fractional reaction–diffusion models with the Riesz fractional derivative. *Mathematics and Computers in Simulation, 202*, 149–163. https://doi.org/10.1016/j.matcom.2022.05.037

Ellahi, R., Zeeshan, A., Hussain, F., & Asadollahi, A. (2019). Peristaltic blood flow of couple stress fluid suspended with nanoparticles under the influence of chemical reaction and activation energy. *Symmetry, 11*(2), 276. https://doi.org/10.3390/sym11020276

Ghasemi, B., Aminossadati, S. M., & Raisi, A. (2011). Magnetic field effect on natural convection in a nanofluid-filled square enclosure. *International Journal of Thermal Sciences, 50*, 1748–1756. https://doi.org/10.1016/j.ijthermalsci.2011.04.010

Han, C., Wang, Y. L., & Li, Z. Y. (2022). A high-precision numerical approach to solving space fractional Gray–Scott model. *Applied Mathematics Letters, 125*, 107759. https://doi.org/10.1016/j.aml.2021.107759

Hayat, T., Khan, M. I., Farooq, M., Alsaedi, A., Waqas, M., & Yasmeen, T. (2016). Impact of Cattaneo–Christov heat flux model in flow of variable thermal conductivity fluid over a variable thickness surface. *International Journal of Heat and Mass Transfer, 99*, 702–710. https://doi.org/10.1016/j.ijheatmasstransfer.2016.04.016

Horváth, G., Horváth, I., Almousa, S. A.-D., & Telek, M. (2020). Numerical inverse Laplace transformation using concentrated matrix exponential distributions. *Performance Evaluation, 137*, 102067. https://doi.org/10.1016/j.peva.2019.102067

Hussain, S., Murtaza, M. G., & Nadeem, S. (2019). Influence of hybrid nanoparticles on the peristaltic flow of Carreau fluid in a non-uniform tube. *Computer Methods and Programs in Biomedicine, 177*, 141–152.

Imoro, I., Etwire, C. J., & Musah, R. (2024). MHD flow of blood-based hybrid nanofluid through a stenosed artery with thermal radiation effect. *Case Studies in Thermal Engineering, 59*, 104418. https://doi.org/10.1016/j.csite.2024.104418

Isah, A., Musa, A., Yakubu, G., Adamu, G. T., Mohammed, A., Baba, A., Kadas, S., & Mahmood, A. (2024). The impact of heat source and chemical reaction on MHD blood flow through permeable bifurcated arteries with tilted magnetic field in tumor treatments. *Computer Methods in Biomechanics and Biomedical Engineering, 27*(5), 558–569. https://doi.org/10.1080/10255842.2023.2190833

Jamil, D. F., Saleem, S., Roslan, R., Al-Mubaddel, F. S., Rahimi-Gorji, M., Issakhov, A., & Din, S. U. (2021). Analysis of non-Newtonian magnetic Casson blood flow in an inclined stenosed artery using Caputo–Fabrizio fractional derivatives. *Computer Methods and Programs in Biomedicine, 203*, 106044. https://doi.org/10.1016/j.cmpb.2021.106044

Jamil, M., Khan, M., Khan, W. A., & Ayaz, M. (2016). Unsteady MHD flow of viscoelastic fluid in a channel with heat and mass transfer. *AIP Advances, 6*(3), 035214.

Khanafer, K., Vafai, K., & Lightstone, M. (2003). Buoyancy-driven heat transfer enhancement in a two-dimensional enclosure utilizing nanofluids. *International Journal of Heat and Mass Transfer, 46*(19), 3639–3653. https://doi.org/10.1016/S0017-9310(03)00156-X

Khan, M., Shah, F., & Islam, S. (2015). Effects of chemical reaction on MHD mixed convection flow of nanofluid over a stretching sheet. *Journal of the Taiwan Institute of Chemical Engineers, 50*, 119–128.

Kot, P., & Elmabound, A. (2021). Analysis of pulsatile blood flow through a stenosed artery using fractional calculus. *Mathematics, 9*(3), 210.

Mahanthesh, B., Gireesha, B. J., & Gorla, R. S. R. (2017). Mixed convection flow of a dusty nanofluid over a stretching sheet embedded in a porous medium with thermal radiation and heat source/sink effects. *Journal of Nanofluids, 6*(4), 702–710.

Nazar, T., & Shabbir, M. S. (2023). Irreversibility analysis in the ternary nanofluid flow through an inclined artery via Caputo–Fabrizio fractional derivatives. *Results in Physics, 53*, 106992. https://doi.org/10.1016/j.rinp.2023.106992

Sandeep, N., & Kumar, B. R. (2016). Effects of inclined magnetic field on flow of a nanofluid over a stretching surface with chemical reaction and radiation. *Journal of Molecular Liquids, 221*, 108–115.

Sheikholeslami, M. (2018). Influence of Lorentz forces on nanofluid flow in a porous cylinder considering Brownian motion. *Journal of Molecular Liquids, 258*, 518–526.

Sheikholeslami, M., & Ganji, D. D. (2016). Ferrohydrodynamic and magnetohydrodynamic effects on ferrofluid flow in a permeable channel with aligned magnetic field. *Journal of Molecular Liquids, 217*, 490–497.

Sheikholeslami, M., Gorji-Bandpy, M., Ganji, D. D., Soleimani, S., & Seyyedi, S. M. (2015). Natural convection of nanofluids in a cavity with thick bottom wall in the presence of magnetic field. *International Journal of Heat and Mass Transfer, 80*, 16–25.

Sheikholeslami, M., & Rokni, H. B. (2017). Nanofluid heat transfer in a permeable cavity considering Brownian motion and thermophoresis effects. *Journal of Molecular Liquids, 233*, 288–296.

Shit, G. C., & Majee, S. (2015). Pulsatile flow of blood and heat transfer with variable viscosity under magnetic and vibration environment. *Journal of Magnetism and Magnetic Materials, 388*, 106–115. https://doi.org/10.1016/j.jmmm.2015.04.026

Tripathi, D., Bég, O. A., & Javed, M. Y. (2018). Unsteady flow of viscoelastic nanofluids in a flexible tube with heat and mass transfer. *Journal of Mechanics in Medicine and Biology, 18*(3), 1850024.

Wang, X., Qiao, Y., Qi, H., & Xu, H. (2022). Numerical study of pulsatile non-Newtonian blood flow and heat transfer in small vessels under a magnetic field. *International Communications in Heat and Mass Transfer, 133*, 105930. https://doi.org/10.1016/j.icheatmasstransfer.2022.105930

Yakubu, D. G., Abdullahi, I., & Musa, A. (2025). The dynamic flow of ternary nanofluids with magnetic nanoparticles in an inclined artery exposed to thermal radiation and magnetic fields. *Alexandria Engineering Journal, 123*, 231–241. https://doi.org/10.1016/j.aej.2025.01.056